Low temperature plasticity and dislocation creep of Fangshan dolomite

Jianfeng Li, Tongbin Shao*, Maoshuang Song**

State Key Laboratory of Isotope Geochemistry, Guangzhou Institute of Geochemistry, Chinese Academy of Sciences, Guangzhou, 510640, China

*,** Corresponding authors: tshao@gig.ac.cn (Tongbin Shao), msong@gig.ac.cn (Maoshuang Song)

Abstract: In order to explore the cause behind a recently so-called inversion of activation energy between dislocation-diffusion creep, we compress Fangshan dolomite at effective pressures of 50-300 MPa, temperatures of 27-900 ℃, and strain rates of 10^{-6}-2×10^{-4} s^{-1} using a Paterson-type apparatus. Two end-member deformation regimes, each with respective diagnostic flow law and microstructure, are recognized. At T≤500 ℃, low temperature plasticity (LTP), expressed by an exponential constitutive equation $\dot{\varepsilon}=\dot{\varepsilon}_0\times\exp(\alpha\times\sigma)$ with $\alpha=0.081\pm0.0078$ and $\ln\dot{\varepsilon}_0=-76.66\pm6.24$, was determined with weakly strain rate dependence and thermal hardening of the strength, and microstructures of predominant undulatory extinctions or f-twinning (Regime 1). At T≥800 ℃, dislocation creep, described by a power law equation ($\dot{\varepsilon}=A\sigma^n\exp\left(\frac{-Q}{RT}\right)$ with $n=4.75\pm0.58$, $Q=436\pm54$ kJ/mol and $\log A=3.48\pm1.41$), was defined with significant strain rate and temperature sensitivities of strength, and microstructures dominated by smooth undulating extinction and new recrystallized grains (Regime 2). Regime 3, transition from LTP to dislocation creep, is also recognized from ~600 ℃ to 800 ℃ with strain rate dependence of strength changing with temperature and developing microstructures similar to those of regime 2. Overall the medium-grained Fangshan dolomites show similar rheology to coarse-grained Madoc dolomites but a beginning temperature of regime 2 about 50-100 ℃ than the latter, making the

dislocation creep of Fangshan dolomite clearly recognized under the condition that dolomite decomposition has no obvious effect. Extrapolated to nature, dislocation creep is expected to occur in a relatively narrow space undergoing high temperatures and relatively high stresses, instead diffusion creep is expected to dominate the deformation of dolomite in low stress tectonic settings.

Keywords: Dolomite, Low temperature plasticity, Dislocation creep, Activation energy, High temperature high pressure, Rheology

1. Introduction

Carbonates, which commonly form and accumulate in shallow-marine environments along continental margins, are distributed extensively in shear zones and orogenic belts in middle and upper crust, and some of them enter the deep Earth during subduction [*Goto et al.*, 2007; *Zhang et al.*, 2003]. Carbonates are believed to control the stresses in the middle and upper crust during continental collision by low strength calcite ($CaCO_3$) and dolomite ($CaMg(CO_3)_2$) [e.g., *Bestmann et al.*, 2000; *Ulrich et al.*, 2002] and play a potential role in the geodynamics of ultrahigh pressure (UHP) metamorphic terranes, mantle wedge, and subduction zones by the mechanical properties of magnesite ($MgCO_3$) [*Holyoke et al.*, 2014]. Obviously, it is of great importance to study the mechanical properties of all carbonates in the Mg-Ca system for understanding the strain and stress distributions in the middle and upper crust and deep Earth.

Ca end-member carbonate, calcite, Mg end-member carbonate, magnesite, and their intermediate (Mg:Ca = 1:1) composition, dolomite, all have a rhombehedral crystal structure with the crystal symmetry ($R\bar{3}c$) of the two end-members distinct from that ($R\bar{3}$) of the intermediate. The similarity and difference of crystal structure and symmetry of the three carbonates imply that mechanical properties of the end-members may be comparable and the flow strength of the three carbonates are expected to related to their magnesium content and shear moduli [*Holyoke et al.*, 2014].

Rheological behaviors and deformation mechanisms of calcite aggregates have attracted extensive research interest [e.g., *Austin and Evans*, 2009; *de Bresser*, 2002; *de Bresser et al*., 2005; *Freund et al*., 2004; *Gratier et al*., 2011; *Griggs and Miller*, 1951; *Griggs et al*., 1953; *Handin and Griggs*, 1951; *Heard and Raleigh*, 1972; *Herwegh et al*., 2003, 2005; *Renner et al*., 2002; *Rutter*, 1972, 1974; *Rybacki et al*., 2011, 2013; *Schmid et al*., 1977, 1980; *Song et al*., 2014; *Turner et al*., 1956; *Walker et al*., 1990; *Xu et al*., 2009, 2010; *Zhang and Zhou*, 2012; *Zhang et al*., 2017]. Of these, the strength of calcite deformed by dislocation creep increased with increasing magnesium content [*Xu et al*., 2009], implying that in the dislocation creep regime the Mg end-member carbonate, magnesite, should be stronger than the intermediate, dolomite, which instead should be stronger than the Ca end-member carbonate, calcite. This was proved recently by *Holyoke et al*. [2014] in which magnesite was shortened in both Heard gas-medium apparatus and Griggs-type solid-medium apparatus to determine its three deformation mechanisms (Low temperature plasticity (LTP), diffusion creep, and dislocation creep) and corresponding flow laws [*Holyoke et al*., 2014]. In contrast to magnesite, although much more high temperature deformation experiments were performed on single crystals [e.g., *Barber and Wenk*, 1979, 2001; *Barber et al*., 1981] and polycrystalline aggregates [e.g., *Davis et al*., 2008; *Delle Piane et al*., 2008; *Heard*, 1976; *Holyoke et al*., 2013; *Neumann*, 1969] of the intermediate, dolomite, there are some debates or doubts. For example, in order to determine the rheological behavior and flow law of coarse-grained dolomite aggregates deformed by dislocation creep, *Holyoke et al*. [2013] performed a series of triaxial compression deformation in a modified-type Griggs apparatus and obtained a significantly low activation energy (Q=145 kJ/mol) for dislocation creep [*Holyoke et al*., 2013] relative to that (Q=410 kJ/mol) for dislocation creep with assuming n=7 and that (Q=280 kJ/mol) for diffusion creep [*Davis et al*., 2008]. Notably, there is a large discrepancy in activation energy for dislocation creep determined from these two studies, and such large difference also occurs in activation energy of dislocation creep between the two end-member carbonates and the intermediate. For this, however, there is no a reasonable interpretation. In addition, such an inversion of activation energy between dislocation

and diffusion creep is obviously unusual since it is generally accepted that rate-limiting mechanisms of intracrystalline deformation will be controlled by larger energy landscape (activation barriers) relative to grain boundary processes such as grain boundary sliding and diffusion creep. It is therefore necessary to perform further research to explore the rate-limiting processes of diffussion and dislocation creep of dolomite, thereby helping us to understand the cause behind the inversion of activation energy.

In this study, we performed a set of triaxial compression experiments at effective confining pressures of ~50-300 MPa, temperatures of 27-900 ºC and strain rates of 10^{-6}-2×10^{-4} s^{-1} in a Paterson-type apparatus to explore the deformation mechanisms and rheological behaviors of medium-grained Fangshan dolomite polycrystalline aggregates.

2. Experimental Methods

A series of triaxial compression experiments were conducted to determine the dependences of flow stress on strain rate and temperature. Microstructures of dolomite aggregates before and after deformation were identified in ultra-thin polished sections (~10 μm) by a Leica optical microscope to document the deformation mechanisms.

2.1. Starting Materials

A white Fangshan dolomite block was collected from a quarry locating in Shiwo town, Fangshan district, Beijing, China. The block is of homogenous structure without obvious mineral bands or foliations, and comprised of primary dolomite (>97 vol.%), secondary calcite, mica and apatite. Chemical compositions were obtained by an EMP analysis with a stoichiometric molecular formula of Mg/Ca ratios between 0.97 and 1.02 (Table 1). Optical examination on this material (Figure 1a) displays approximately equant grains with diameter determined as 113±42 μm by linear traverses of the thin section under optical microscopy (Figure 1b). As shown in Figure 1a, sharp boundaries, uniform extinction and some straight boundary twin can be observed, and negligible porosity of less than 1% can be estimated. Neither banding nor foliation has been observed in hand specimen, but pole figures (Figure 2) generated by Electron

Backscatter Diffraction (EBSD) analysis display a weak initial fabric with maximum c-axis densities about two times the expected mean density for random distributions.

2.2. Sample Preparation and Jacketing

Specimen cylinders of 10 mm diameter and 20 mm length were core-drilled from a block of the Fangshan dolomite. The top and bottom surfaces of the cylinders were polished to roughness of less than ±5 μm. Before each test, the cylindrical specimens were dried for at least 24 hours in an oven at 110 ℃ in order to drive away free water, and then sandwiched between 3 mm thick solid alumina spacers, additional 58 mm long alumina and 30 mm long zirconia pistons to insure a good thermal profile along the longitudinal direction of sample (Figure 3). The assembly was sealed in low carbon iron jackets with 0.25 mm wall thickness and 15 mm inner diameter in order to isolate the sample from the confining medium of argon gas. In the central part glued to the specimen, the jacket was swaged down to 10 mm, which resulted in local thickening up to a maximum of ~0.4 mm.

2.3. Deformation Experiments

The triaxial compression experiments were performed on dolomite aggregates under ~50-300 MPa effective confining pressure and ~27-900 ºC temperatures in an internally heated Paterson gas-medium (argon) deformation apparatus [*Paterson*, 1970; *Shao et al*., 2011]. The temperature distributions inside the furnace were regularly calibrated to make sure that the thermal profiles were nearly constant (within ± 2 ℃) along the longitudinal direction of sample. Temperatures were monitored by a R-type (Pt13%Rh-Pt) thermocouple placed about 3 mm above the top surface of the specimen. Temperature was increased at a rate of 20 ℃ per minute to the testing temperature, and then maintained 30 minutes for equilibrium. Details of the deformation apparatus and data processing can refer to *Shao et al*. [2011] and *Li et al*. [2013], respectively. In order to obtain the flow laws and explore the rheological behaviors of dolomite, two types of tests were employed:

(1) Constant strain rate tests. Indeed, we drive the motor at a constant displacement speed during the whole deformation process. Since a constant flow stress was soon approximately reached after a transient elastic period (generally less than about 3%

strain) in most tests, the main part of the test was at approximately constant strain rate.

(2) Strain-rate-stepping tests. The stepping tests comprise of a series of steady flow at various strain rates. Generally, we performed these tests by abruptly increasing the strain rate after the specimen had settle down to a steady flow at the previous strain rate.

The testing conditions (include temperature, confining pressure, and strain rate) and mechanical results of the experiments were listed in Tables 2 and 3, respectively, for the constant strain rate tests and steeping tests. For specimens deformed at relatively low temperatures and without undergoing strain-weakening, differential stresses at 5% strains were adopt as flow stresses of the specimens. If the total strain for the constant strain rate tests or each step of stepping tests was less than 5%, a power function used to fit the strain hardening after yield point can be written as

$$\sigma = A \times (\varepsilon - b)^m$$

and extrapolated to 5 % strain where differential stress was read and considered as flow stress. In the function, σ and ε are real-time differential stress and strain, respectively; *A*, *b* and *m* are fitting parameters and *m* is closely related to the strain hardening degree of the specimen. For specimens undergoing strain weakening at high temperature, however, peak differential stresses were considered as flow stresses.

Additionally, as the ceramic spacers beneath the specimen were solid without central hole, the gas produced by dolomite decomposition (generates calcite, periclase and CO_2) at high temperatures (≥ ~700 °C) could not escape from the assembly and thus generated pore fluid pressure. As mentioned above, the porosity of the starting material (Fangshan dolomite) was less than 1%, little decomposition at grain surfaces of the dolomite would reach equilibrium. Hence, the stability of the dolomite can be maintained in the laboratory on the basis of the above facts and microstructure observations. According to the decomposition reaction equilibrium of dolomite presented by *Goldsmith* [1959], CO_2 pore pressure at different temperatures could be obtained, and the effective confining pressure could be expressed by

$$P_e = P_c - P_{CO_2}$$

where P_e, P_c and P_{CO_2} represent the effective confining pressure, confining

pressure and pore fluid pressure generated by CO_2, respectively.

As the confining pressure of tests in this work were mostly fixed at ~300 MPa, the effective confining pressure would be various once the decomposition of the dolomite grains occurred at different deformation temperatures. In order to obtain flow stress corresponding to a constant confining pressure (P_c) for building constitutive equation, the following corrections should be emphasized:

It was suggested by *Davis et al*. [2008] that flow stress of Madoc dolomite depends linearly on effective confining pressure with tiny apparent coefficient of inner friction about 0.1 ($\mu \cong 0.1$) if deformed at P_e > 100 MPa, 700 ℃ and strain rate of 1.25×10^{-5} s^{-1}, while if P_e < 100 MPa the dependence of flow strength on effective confining pressure met Mohr – Coulumb Criterion with apparent coefficient of inner friction about 1.0 ($\mu \cong 1.0$) (Figure 4). Similar dependent relationships were also reported in other studies [e.g., *Austin and Kennedy*, 2005; *Austin et al*., 2005; *Handin and Fairbairn*, 1955; *Turner et al*., 1954]. Our experimental results of samples FS34 and FS26 deformed at P_e > 100 MPa, 800 ℃ and strain rate of 10^{-5} s^{-1} indicate that flow strengths of Fangshan dolomite have a similar dependent relationship on effective pressure to Madoc dolomite. Accordingly, for tests in which dolomite decomposed, if $P_e \geq 100$ MPa, the flow strength was corrected by:

$$\sigma_t = \sigma_{5\%} + 0.1\times\left(300 - P_e\right) \qquad (1)$$

where σ_t is the true flow strength corresponding to effective confining pressure of 300 MPa; $\sigma_{5\%}$ is the differential stress read at 5% strain; P_e is the effective confining pressure. If P_e <100 MPa, the true flow strength can be obtained by:

$$\sigma_t = \sigma_{5\%} + \left(100 - P_e\right) + 0.1\times\left(300 - 100\right) \qquad (2)$$

The corrected flow stress corresponding to effective confining pressure of 300 MPa was filling into antepenultimate column of Tables 2 and 3.

At last, power law and exponent law constitutive equations were fitted to the mechanical data of the tests at higher and lower temperatures, respectively.

2.4. Microstructure Observations

Specimens deformed at various strain rates and temperatures were inspected to characterize their deformation microstructures by a Leica microscopy in parallel-polarized light and cross-polarized light. The specimens were impregnated with an epoxy resin and then cut in half along the compression direction. One half was polished to thin sections of about 10 μm thick. Microcracks can be judged in parallel-polarized light micrographs. In contrast, mechanical twinning, undulating extinctions, deformation bands and recrystallization grains can be observed in cross-polarized light micrographs.

3. Results

3.1. Mechanical Data

The mechanical results of constant strain rate and strain-rate-stepping tests are listed in Tables 2 and 3, respectively. Differential stress versus strain curves for constant strain rate and strain-rate-stepping tests are displayed in Figures 5 and 6, respectively. According to strain rate and temperature dependences of flow stress, three deformation regimes have been distinguished by temperature bounds as follows:

Regime 1 (≤ 500 ℃). In this regime, the Fangshan dolomites yield when differential stresses lie between ~352 and 501 MPa at strains 0.5%-1%. Once reaching yield point, the differential stress versus strain curves (Figures 5 and 6) deviate from linear relationship and show various degrees of strain hardening (depending on temperature). It was found that specimens deformed at 500 ℃ had the most obvious strain hardening (Figure 5a). Differential stresses at 5% strain of sample deformed in regime 1 arrive between ~765 and 832 MPa. Flow stresses show weak dependences on temperature and strain rate (Figure 5a). For instance, the increase of flow stresses with strain rate increasing were too slight to escape from being covered up by strain hardening and/or strength discrepancy likely resulting from microstructure difference among specimens. Thus, it is necessary for strain-rate-stepping tests being carried out on a single specimen to eliminate the effect of microstructure discrepancy. From logarithmic graph of strain rate versus flow stress (Figure 7a), linear dependent relationships with dramatically steep slopes (apparent n) of 70-78 were identified.

Increasing experimental temperatures from room temperature to 300 ℃, flow strengths of the Fangshan dolomite become weakly lower or nearly invariant; while increasing temperatures from 300 ℃ to 500 ℃, the flow strengths increase slightly (Figure 8). This unusual temperature dependence cannot be described by an Arrhenius relationship. Thus, an exponential law without Arrhenius factor:

$$\dot{\varepsilon}=\dot{\varepsilon}_0 \times \exp\left(\alpha \times \sigma_{5\%}\right) \qquad (3)$$

was used to fit the mechanical results in regime 1. In equation (3), $\dot{\varepsilon}$ is strain rate, pre-exponential terms $\dot{\varepsilon}_0$ is in units of strain rate (s^{-1}), $\sigma_{5\%}$ is the differential stress read at 5% strain, α (MPa^{-1}) is fitting parameter. By multiple least square fitting of experimental results at room temperature to 300 ℃, parameters in equation (3) can be determined as $\alpha = 0.081 \pm 0.0078$ and $\ln \dot{\varepsilon}_0 = -76.66 \pm 6.24$. Fitting of mechanical data of 500 ℃ gives nearly same $\alpha\ (=0.084)$ and $\ln \dot{\varepsilon}_0\ (=-80.23)$.

② Regime 2 (≥ 800 ℃). This regime refers to experiments at temperatures higher than 800 ℃ and/or low strain rate ($\leq 1.0\times10^{-5}$ s^{-1}) at 800 ℃, and is characterized by low flow stresses not higher than ~520 MPa. In this regime, the yield strengths of Fangshan dolomite were much lower, strain hardening after the yield point was inconspicuous, instead strain weakening on differential stress versus strain curves are observed after ~3%-6% strain (Figures 5c and 5d). At *T*=850 ℃, strain weakening of dolomite is generally prominent with significant stress drop occurring at strains of ~3%-4%. Corrected flow strengths of Fangshan dolomite are 204 to 518 MPa, and increase much more significantly with increasing strain rates, apparently different from regime 1. In the logarithmic diagram of strain rate versus differential stress, flow strengths of constant strain rate experiments (peak stresses of each test) are consistent well with that of strain-rate-stepping experiments where differential stresses are read for each step as near as possible to 5% strain although some scatter may be present. Linear relationships between strain rate and flow strength have more gentle slopes of 3.8 – 5.4 (Figure 7c), basically consistent with the expected values of stress exponent for dislocation creep. Increasing or decreasing temperature, flow strengths decrease or increase more

obviously than those for samples deformed at temperature lower than 600 ℃. In a diagram of logarithmic flow strength versus 1000/T (Figure 8a), significant positive linear dependence of steeply inclined slope ($\rho = \frac{Q * \log \sigma}{nR} = 4.82 - 4.86$ in Figure 8b) is determined at high temperatures (≥ 800 ℃), obviously different from the approximately horizontal slope at temperatures lower than 600 ℃.

Power law with Arrhenius factor could describe well the rheological behavior at high temperatures with the formation as:

$$\dot{\varepsilon} = \mathrm{A} \times \sigma^{n} \exp\left(\frac{-Q}{RT}\right) \qquad (4)$$

where $\dot{\varepsilon}$ is strain rate, A is the pre-exponential term, R is the gas constant, Q is the active energy, T is absolute temperature in K, n is fitting parameter indicative of stress exponent, and σ is the flow stress corresponding to $P_e = 300$ MPa in this study. For individual constant strain rate experiments, peak stresses are adopted as flow stresses; while in strain-rate-stepping experiments differential stresses read at strains as near as possible to 5% are considered as flow stresses of each step. By multiple least square fitting of experimental results of flow stresses lower than 520 MPa, parameters in equation (4) can be determined as n=4.75±0.58, Q=436±54 kJ/mol and log$A$=3.48±1.41.

A transitional regime (Regime 3) from regime 1 to regime 2 is also recognized at temperatures between 500 ℃ and 750 (800) ℃. In this regime, increasing strain rate, flow stresses will increase more significantly than in regime 1 but not as significantly as in regime 2. Lower than regime 1 but higher than regime 2, the slopes of linear relationship between logarithmic strain rate and logarithmic flow stress for the transitional regime range from 48 to 13 (11) (Figure 7b). A corresponding transitional stress dependence on temperature can also be recognized in Figure 8a, indicated by cambered distribution of data points. As the apparent n values are much higher than the values expected for dislocation creep [3≤n≤5, *Poirier,* 1985] and decrease with increasing temperature, the deformation mechanism of the regime 3 should be dominated by dislocation glide with little effect of recovery on dislocation creep, the process transition from grain boundary sliding to high temperature intracrystalline

plasticity.

3.2. Microstructures

The deformation microstructures of Fangshan dolomite at the optical scale are distinguished briefly in the above three deformation regimes.

(1) Specimens deformed in regime 1 (≤ 500 ℃)

Optical observations reveal a preponderance of mechanical twining (Figures 9c-9f) in this regime. The twins produced by deformation were of lensoid shape, with sharp ends at grain boundaries. This characteristic lamellae shape makes them easily distinguishable from the straight lamellae boundaries which may be initially present or produced by quenching during cooling and depressurizing at the end of the experiment. Besides twining, some grains show undulatory extinction (Figures 9a, 9b, and 9d). The mutual developments of mechanical twinning and undulatory extinction indicate the dolomite is deformed by a combination of twinning and dislocation slip. In more detail, specimen deformed at room temperature is characterized by patchy undulatory extinction with small amount of twins. With increasing temperature, the population of twins increases. For instance, specimens at 300 ℃ develop much more abundant deformation twins, while the most popular twins are discovered in specimens deformed at 500 ℃. The differential stresses reached at low temperatures ≤500 ℃ are much higher than the confining pressures, brittle processes thus may contribute to deformation of dolomite according to the Goetze criteria [*Karato*, 2008]. However, no more significant micro-cracks than the starting materials have been ferreted out.

(2) Specimens deformed in regime 2 (≥800 ℃)

Fangshan dolomites deformed at temperatures ≥800 ℃ have smooth undulatory extinctions (Figures 10a-10b) and similar twin density with the starting materials. Some dust like fine grains is discovered at the triple junction of dolomite grains or surrounding the accessory minerals such as mica and apatite (Figures 10c). EMP analyses suggest that these new grains are formed due to the lost MgO content of dolomite, consistent with decomposition products of dolomite in a previous study by *Delle Piane et al.* [2008]. The present of these new fine grains indicates that CO_2 has been released from some old grains. As the reaction areas are less than 2% in our samples, however,

differential stresses measured earlier in the experiments should be able to represent the flow stresses of the dolomite after corrected. Along some old and coarse dolomite grains, fine grains with equiaxed polygonal shape are also discovered, which should be the recrystallized new grains formed by dislocation climb and distinguished from reaction products with coarser grain size and colorful optical character (Figure 10d).

(3) Specimens deformed in regime 3 (~500 ℃<T<800 ℃)

Specimens deformed at temperatures from 500 ℃ to 800 ℃ have similar microstructures to those deformed at temperatures higher than 800 ℃ with the exception of no or less new fine grains generated by decomposition of dolomite.

4 Discussion

Dolomite has similar crystal structure to calcite and magnesite, with half Ca octahedron in calcite replaced orderly by Mg octahedron or with half Mg octahedron in magnesite replaced orderly by Ca octahedron. Experimental studies of rheological properties of dolomite are much less than calcite, but much more compared to magnesite. However, disputes or doubts on the rheology of dolomite are attractive. In the last century, most experimental studies on dolomite deformation were performed at low temperatures (<500 ºC) [e.g., *Barber et al.*, 1994; *Handin and Fairbairn*, 1955; *Turner et al.*, 1954], but there are some exceptions. Although at a much higher temperature (1000 ºC), for instance, *Neumann* [1969] suggested that dislocation creep was the dominant deformation mechanism of coarse-grained (~700 μm) dolomite aggregates based on microstructural evidences obtained, he did not determine flow laws of dolomite due to poor precision of strong solid-media assemblies in the Griggs-type deformation apparatus. Using high-precision gas-medium Heard and modified-type Griggs apparatus, deformation experiments on coarse-grained Madoc dolomite and fine-grained synthetic dolomite aggregates were carried out recently at temperatures higher than 700 ℃ [*Davis et al.*, 2008; *Delle Piane et al.*, 2008; *Holyoke et al.*, 2013]. These previous studies could be compared mutually with similarity and difference both in yield strength and flow strength between different studies [e.g., *Barber et al.*, 1994; *Davis et al.*, 2008; *Handin and Fairbairn*, 1955; *Turner et al.*, 1954]. For comparison,

some differential stress versus strain curves documented by these previous studies were also plotted in Figure 5a according to their deformation temperatures. At low temperatures of ≤300 °C, Hasmark dolomite [*Handin and Fairbairn*, 1955] and Crevola dolomite [*Barber et al.*, 1994] display flow strength increasing with decreasing temperature. The same is true for our Fangshan dolomite deformed at temperatures ≤300 °C, where at the same strain rate (10^{-5} s^{-1}) sample FS5 deformed at room temperature is stronger than sample FS7 shortened at 300 °C (Figure 5a). This is also true for samples compressed at temperatures ≥500 °C. For instance, the flow strength of sample FS8 deformed at 500 °C and 7.8×10^{-6} s^{-1} is much higher than that of sample FS10 deformed at 700 °C and 1.7×10^{-6} s^{-1}. From 300 °C to 500 °C, however, an unusual increase in flow strength of Fangshan dolomite occurs with increasing temperature (Figure 5a), which is similar with the dependence of flow strength of coarse-grained Madoc dolomite on temperature at low temperatures ≤700 °C (see Figure 2b of *Davis et al*. [2008]). At relatively low temperatures (≤500 °C), in addition, the the Fangshan dolomites yield at 352–369 MPa and their flow stresses are 765–804 MPa when deformed at 300 °C, while the Hasmark dolomites shortened by *Handin and Fairbairn* [1955] yield at 364 MPa and have a flow stress of 660 MPa. This inversion of strength of coarse-grained and finer-grained dolomite also occurs between the medium-grained Fangshan dolomite (FS8) and coarse-grained Madoc dolomite (MD26) when deformed at low temperatures (Figure 5a). When compared to previous studies, *Davis et al*. [2008] also found this strength inversion that the fine-grained synthetic dolomite is stronger than the coarse-grained Madoc dolomite at a temperature of 600 °C, and the fine-grained Blair dolomite exhibits flow strength much higher than the coarse-grained Madoc dolomite at temperatures ≤500 °C. Thus, these comparisons suggest that the fine-grained dolomite was stronger than the coarse-grained dolomite, at relatively low temperatures (≤500 °C for the comparisons of Fangshan or Blari dolomite with Madoc dolomite, and ≤600 °C for those of fine-grain synthetic dolomite with Madoc dolomite). Additionally, the insensitivity of flow strength to the strain rate occurs at temperatures (≤500 °C) for our medium-grained Fangshan dolomite about 200 °C lower than those (≤700 °C) for the coarse-grained Madoc dolomite [*Davis et al.*, 2008]. This

insensitivities result in abnormally large stress exponents (n=~70 for Fangshan dolomite and ~46 for Madoc dolomite) for these low temperature deformation experiments.

4.1. Deformation Mechanisms and Flow Laws

Microstructure observations of the deformed specimens suggested that dislocation glide is the most important deformation mechanism at room temperature to 300 ºC, while f-twin slip became more dominant at 300-500 °C. At temperatures >~700 °C, dislocation creep became the dominant deformation mechanism. In the light of the critical resolved shear stress (CRSS) of dolomite single crystal [Figure 11; *Barber et al*., 1981; *Higgs and Handin*, 1959], at temperatures lower than 500 ℃ CRSS for c slip was the lowest, at temperatures from 500 ℃ to 700 ℃ CRSS for f-twin slip became the lowest one, while at temperatures higher than 700 ℃ CRSS for f slip turns to be the lowest. Thus, the transient of deformation mechanism of Fangshan dolomite from c slip at room temperature to f-twinning at 500 °C was consistent with the trending in change of CRSS of single crystal dolomite. Deformed by dislocation glide and f-twinning at low temperatures ≤500 °C, strength inversion of fine-grained dolomite and coarse-grained dolomite is consistent with a generally accepted theory that grain boundaries impede dislocation motion, and at least at lower temperatures, finer grain size (larger grain boundary area) usually results in higher strength [e.g., *Wright*, 2016]. However, mechanical data at temperatures higher than 700 ℃ show that the deformation mechanism of Fangshan dolomite is dominated by dislocation creep instead of f slip. At temperatures ≥800 °C, the dependence of flow stress on temperature was much more significant than that of CRSS of f-slip (Figure 11), also suggesting that recovery may play an important role in the deformation of the Fangshan dolomite. Furthermore, the CRSSs for both c- and f-twin slips increase with temperature increasing, that is the reason why the flow strength of Fangshan dolomite show slightly overall ascending tendency from room temperature to 500 °C.

Previous studies have recognized several deformation and recovery mechanisms by TEM analysis of single crystal and polycrystalline aggregate of dolomite [e.g., *Barber et al*., 1981, 1994; *Barber and Wenk*, 2001]. In Crevola dolomite, for instance,

f twin has been observed at 25 °C≤T≤500 °C, $\dot{\varepsilon}=10^{-4}$ s^{-1} and 700 °C≤T≤900 °C, $\dot{\varepsilon}=10^{-6}$ s^{-1} [*Barber et al.*, 1994]. However, the densest f twin was found to develop in the temperature range from 500 °C to 700 °C. In contrast, c slip and f slip were active at all of temperatures, and f slip became more active at temperatures ≥700 °C. All of these observations were consistent with the mechanical data and microstructures of the Fangshan dolomite. In conclusion, intracrystalline plasticity deformation at high stresses and low temperatures ≤500℃ should be dominated by the coaction of f–twin and c–slip; the drastic strength decrease at temperature ≥700 °C was likely resulted from the CRSS decrease of f – slip as well as the activation of dislocation recovery.

The flow laws of dolomite aggregates were reported with the constitutive equation for diffusion creep with n = 1.28, H^*=280 kJ/mol [*Davis et al.*, 2008] and n=1.3, H^*=368 kJ/mol [*Delle Piane et al.*, 2008], respectively. However, an activation energy of 310 kJ/mol was obtained by *Holyoke et al.* [2013] from Figure 7 of *Delle Piane et al.* [2008]. Thus, the data on flow laws of diffusion creep determined by these two studies are essentially the same within experimental errors. Report about LTP and dislocation creep was scare. *Davis et al.* [2008] experimentally studied the deformation of coarse-grained Madoc dolomite from 400 ℃ to 850 ℃. Exponential law with $\alpha=0.079\pm0.01$ MPa^{-1} and power law with n=26±6 and $\frac{H^*}{n}=60\pm6$ kJ/mol were obtained to describe the LTP and dislocation creep of dolomite, respectively. Because the stress exponent was abnormally high for dislocation creep, *Davis et al.* [2008] adopted the n value (n=7) of Carrara marble [*Schmid et al.*, 1980] to calculate the activation enthalpy of the Madoc dolomite, by which a more reasonable value of H^*=~410 kJ/mol was gotten. However, another suit of parameters of n=3.0±0.1 and H=145 kJ/mol was reported recently by *Holyoke et al.* [2013] for dislocation creep. How does such a large difference in activation energy occur between the two studies? Detail experimental works in this study show that:

1) The stress exponent for the Fangshan dolomite deformed at 850 ℃ is determined as 3.8 (Figure 7c), nearly consistent with the stress exponent value (n=3.0±0.1) obtained for Madoc dolomite deformed at 900 ℃ by *Holyoke et al.* [2013].

According to the dislocation creep theories [*Poirier*, 1985], the deformation of Fangshan dolomite at 850 ℃ is controlled by a dislocation creep dominant deformation process. For this reason, a beginning temperature of dislocation creep may be lower for the medium-grained Fangshan dolomite relative to the coarse-grained Madoc dolomite.

2) Overall fitting of data points of logarithmic strain rate and logarithmic stress for the Fangshan dolomite deformed at 800 ℃ generates a value of n=7.8, almost equal to the stress exponent value assumed previously for the dislocation creep of Madoc dolomite by *Davis et al*. [2008]. At 800 ℃, however, respective fitting of data points for flow strengths higher than 520 MPa and lower than 520 MPa produces n = 11.3 and n = 5.4, respectively. This means that the deformation of dolomite at 800 ℃ should be mixture of regime 2 dislocation creep - dominant deformation and regime 3 dislocation slip - dominant deformation. For the deformation of coarse-grained Madoc dolomite, same n value (n=49) was reported for experiments at 600 and 700 ºC, while a lower n value (n=26) was required to fit the mechanical data at 800 ºC, implying a possible transition of deformation mechanism at 800 ºC [*Davis et al*., 2008]. However, the stress exponent (n=7) assumed by *Davis et al*. [2008] for the deformation of the coarse-grained Madoc dolomite at this temperature is still large relative to the values (n=3-5) expected for dislocation creep. This is why *Holyoke et al*. [2013] obtained n=3 of the coarse-grained Madoc dolomite only at a higher temperature (T=900 ºC). In contrast, a decrease in stress exponent of Fangshan dolomite with increasing temperature occurs from 600 ºC to 750 ºC at which the stress exponent value (n=13) is nearly equal to that (n=11) at 800 ºC where flow strength is higher than 520 MPa (Figure 7b). Therefore, it is suggested that the beginning temperature of dislocation creep for medium-grained Fangshan dolomite is about 50-100 ºC lower than that for coarse-grained Madoc dolomite.

3) Fitting of data points of logarithmic strain rate and logarithmic stress for flow strength lower than 520 MPa gives n = 5.4 for deformation of dolomite at 800 ℃ and low strain rate and n = 3.8 for that at temperatures ≥850 ℃. These n values are basically in the range of stress exponent values expected for dislocation creep (n =3-5). Therefore, the deformation under differential stress less than 520 MPa should be dominated by

dislocation creep. Global fitting of power flow law to mechanical data with differential stresses less than 520 MPa shows n=4.75±0.58, Q=436±54 kJ/mol and log$A$=3.48±1.41, which can be used to describe the dislocation creep of the Fangshan dolomite. Stress exponent and activation energy obtained here may be more reasonable according to the following analyses. Firstly, as an intermediate of carbonate in Ca-Mg system, dolomite has a similar crystal structure to the two end-member carbonates, calcite and magnesite. Therefore, similarity in both flow laws and deformation mechanisms may be present among these three carbonates. Secondly, the stress exponent (n) value of the medium-grained Fangshan dolomite is roughly consistent with the value of Carrara marble (n=4.2) [*Schmid et al*., 1980] and is within the value of stress exponent expected for dislocation creep, although it is slightly higher than that of coarse-grained Madoc dolomite (n=3.0±0.1) [*Holyoke et al*., 2013]. Thirdly, the activation energy (Q) determined for the medium-grained Fangshan dolomite is comparable to the values of Q for Carrara marble (Q=428 kJ/mol) [*Schmid et al*., 1980] and magnesite (Q=410 kJ/mol) [*Holyoke et al*., 2014], but is much higher than the value determined for the dislocation creep of coarse-grained Madoc dolomite (Q=145 kJ/mol) [*Holyoke et al*., 2013]. Furthermore, the activation energy obtained by *Holyoke et al*. [2013] is much lower than the value for diffusion creep of dolomite (H^*=~248 kJ/mol) [*Davis et al*., 2008]. In addition to a complicated interpretation, a mechanism suggested by *Barber et al*. [1981] responsible for anomalous hardening of c slip with increasing temperature in the field of crystal plasticity was cited to link with the unusually low activation energy for the dislocation creep deformation of dolomite [*Holyoke et al*., 2013, 2014]. However, c slip leading to anomalous thermal hardening of dolomite is restricted at low temperatures, such as at T≤500 ºC for Fangshan dolomite (Figure 5a), rather than at high temperatures where dislocation creep may dominate. In contrast to the much lower activation energy determined by *Holyoke et al*. [2013], the value of activation energy for dislocation creep of Fangshan dolomite in this study is higher than those for diffusion creep determined by *Davis et al*. [2008] and *Delle Piane et al*. [2008], consistent with a generally accepted knowledge that rate-limiting processes of intracrystalline creep will be controlled by larger energy landscape (activation barriers)

relative to grain boundary process such as grain boundary sliding and diffusion creep.

4.2 Geological Implications

Similar to those for the Madoc dolomite by *Davis et al*. [2008], our experimental results for the Fangshan dolomite can also be used to describe the flow laws for crystal-plastic deformation at low temperatures with an exponential relationship and dislocation creep at high temperatures with a power relationship. In contrast to a higher stress exponent n=7 assumed by *Davis et al*. [2008] and a much lower activation energy Q=145 kJ/mol determined by *Holyoke et al*. [2013] both for dislocation creep, our stress exponent (n=4.75) and activation energy (Q=436 kJ/mol) values are more reasonable and reliable. In order to predict the deformation mechanisms dominating the rheology of medium-grained dolomite aggregates within the Earth, the low temperature exponential law and high temperature dislocation flow law determined in this study and that reported for diffusion creep of fine-grained synthetic dolomite aggregates [*Davis et al*., 2008] are combined to define a deformation mechanism map for dolomite aggregate with a grain size of 100 μm in the logarithm stress versus T/T_m space (Figure 12), where T_m is the melting point of dolomite [*Wyllie and Huang*, 1976]. As the activation energy in our power law for dislocation creep is quite close to the value of *Davis et al*. [2008] but much higher than that of *Holyoke et al*. [2013], our deformation mechanism map is similar to that of *Davis et al*. [2008] but apparently different from that of *Holyoke et al*. [2013]. Compared with the map of *Davis et al*. [2008], a little steeper dislocation creep-diffusion creep boundary is displayed in our map due to relatively more sensitive temperature dependence of strength for Fangshan dolomite than Madoc dolomite. As shown in Figure 12, three fields are distinct in the deformation mechanism map for dolomite with LTP at high stresses, dislocation creep at high temperatures and relatively high stresses, and diffusion creep at low stresses and elevated temperatures. Crystal plasticity and twinning dominate the deformation of dolomite at very high stresses, nearly independent on strain rate. From laboratory to nature, for instance, several orders of magnitude difference in strain rate does not result in a large difference in strength in the field of LTP. In addition, strengths increase slightly with increasing temperature in this field, corresponding to the thermal increase

in CRSS of c-slip [Figure 11; *Barber et al*., 1981]. This is unusual relative to generally accepted temperature dependence of strength for common rock-forming minerals although such thermal hardening was earlier reported by *Davis et al*. [2008] for Madoc dolomite deformed at $T \leq 700$ ºC, by *Higgs and Handin* [1959] and *Barber et al*. [1981] for oriented single crystals of dolomite, and by some much earlier works [e.g., *Ardley*, 1955; *Davies and Stoloff*, 1965; *Lawley et al*., 1961; *Stoloff and Davies*, 1964] for alloys with order-disorder or lattice anisotropy. One possible interpretation by *Barber et al*. [1981] is that the thermal hardening is limited to basal (c) slip and during dislocation movement the increase of friction of CO_3^{2-} groups increases with thermal vibration, expansion and rotation of CO_3^{2-} groups. However, there is no similar thermal hardening found in calcite [e.g., *Barber et al*., 1981, 2007; *de Bresser and Spiers*, 1997] with crystal structure similar to dolomite. Therefore, further research is needed to explore the reasons behind this behavior.

Extrapolated to nature, for dolomite aggregates with a grain size of 100 µm deformed over most geological strain rates (10^{-10}-10^{-14} s^{-1}), LTP dominates at temperatures not higher than ~560 ºC. At temperatures between 560 ºC and 650 ºC, the deformation of dolomites is dominated by LTP at relatively high differential stresses and by diffusion creep at low stresses (Figure 12a). When T>650 ºC, however, diffusion creep is the dominant deformation mechanism, likely accompanied by small amount of LTP and dislocation creep deformation. Given a specific strain rate (10^{-14} s^{-1}) for the deformation of dolomite in nature, change in grain size shifts the diffusion creep-dislocation creep boundary to higher temperatures when coarsening or to lower temperatures when refining (Figure 12b). Depending on grain size, the extent of the dislocation creep field is limited to high temperatures and relatively high stresses (T>~460 ºC for d=1 µm, T>~500 ºC for d=10 µm, T>~560 ºC for d=100 µm, and T>~600 ºC for d=250 µm). This means that dislocation creep is expected to occur in relatively narrow space undergoing high stresses and high temperatures, instead diffusion creep is expected to dominate the deformation of dolomite over most geological strain rates and low tectonic stress environments.

5. Conclusions

Triaxial compression experiments performed on medium-grained Fangshan dolomites at effective pressures of ~50-300 MPa, temperatures of 27-900 ℃, and strain rates from 10^{-6} s^{-1} to 2×10^{-4} s^{-1} roughly define three different deformation regimes: regime 1 dominated by LTP (dislocation slip and f-twining), regime 2 by dislocation creep, and regime 3 by transient state of LTP to dislocation creep. Mechanical data are used to determine the rheological parameters of LTP by an exponential relationship with $\alpha = 0.081 \pm 0.0083$ and $\ln \dot{\varepsilon}_0 = -76.66 \pm 6.24$ and of dislocation creep by a power law relationship with n=4.75±0.58, Q=436±54 kJ/mol and log$A$=3.48±1.41.

Compared with previous studies, our medium-grained Fangshan dolomites show similar rheological behavior to coarse-grained Madoc dolomites but have a beginning temperature of dislocation creep about 50-100 ℃ lower than the latter. In addition, a more reasonable activation energy, higher than those for diffusion creep of fine-grained dolomites determined previously, is obtained for the medium-grained Fangshan dolomite. Flow laws for medium-grained Fangshan dolomite determined in this study and fine-grained synthetic dolomite reported previously are combined to construct a deformation mechanism map for dolomite. Three fields are distinguished with LTP at high stresses and low temperature, dislocation creep at high temperatures and relatively high applied stresses, and diffusion creep at moderate-high temperatures and low stresses. The dislocation creep-diffusion creep boundary shifts to higher temperatures when coarsening or to lower temperatures when refining. Dislocation creep is expected to occur in a relatively narrow space undergoing high temperatures and high stresses, instead diffusion creep is expected to dominate the deformation of dolomite in tectonic settings characterized by most geological strain rates and low stress.

Acknowledgement

We appreciate the critical and constructive comments of the reviewers and the Editor-in-Chief that helped us to improve the manuscript. Dr. Hao Wang is thanked for helping in fielding work and Dr. Guinan Zhang is thanked for help during some

589 experiments. Professor Yongsheng Zhou is gratefully acknowledged for critical
590 comments on an early version of this manuscript. The data supporting the analysis and
591 conclusions is given in Figures and Tables. Original data is accessible through the
592 Mendeley repository (http://dx.doi.org/10.17632/hmmt2797yk.1). This work was supported by
593 the Strategic Priority Research Program (B) of Chinese Academy of Sciences (Grant
594 No. XDB18010402), the National Natural Science Foundation of China (Grant Nos.
595 41572198 and 41702224), and the Pearl River Talent Plan of Guangdong Province. This
596 is a contribution to No. IS-XXXX from the GIGCAS.
597

598 **References**

599 Ardley, G. W. (1955), On the effect of ordering upon the strength of Cu_3Au, *Acta*
600 *Metall., 3*, 525-532.
601 Austin, N., and B. Evans (2009), The kinetics of microstructural evolution during
602 deformation of calcite, *J. Geophys. Res., 114*, B09402,
603 doi:10.1029/2008JB006138.
604 Austin, N. J., and L. A. Kennedy (2005), Textural controls on the brittle deformation
605 ofdolomite: variations in peak strength, In: Gapais, D., Brun, J.P., Cobbold, P.R.
606 (Eds.), Deformation Mechanisms, Rheology and Tectonics: from Minerals to the
607 Lithosphere, *Spec. Publ. Geol. Soc. Lond., 243*, 37–49.
608 Austin, N. J., L. A. Kennedy, J. M. Logan, and R. Rodway (2005), Textural controls on
609 the brittle deformation of dolomite: the transition from brittle faulting to cataclastic
610 flow, In: Gapais, D., Brun, J.P., Cobbold, P.R. (Eds.), Deformation Mechanisms,
611 Rheology and Tectonics: from Minerals to the Lithosphere, *Spec. Publ. Geol. Soc.*
612 *Lond., 243*, 51–66.
613 Barber, D. J., H. C. Heard, and H. R. Wenk (1981), Deformation of dolomite single
614 crystals from 20 °C -800 °C, *Phys. Chem. Miner., 7*, 271–286.
615 Barber, D. J., and H. R. Wenk (1979), Deformation twinning in calcite, dolomite, and
616 other rhombohedral carbonates, *Phys. Chem. Miner., 5*, 141-165.
617 Barber, D. J., and H. R. Wenk (2001), Slip and dislocation behavior in dolomite, *Eur.*
618 *J. Mineral., 13*, 221–243.

619 Barber, D. J., H. R. Wenk, J. Gomez-Barreiro, E. Rybacki, and G. Dresen (2007), Basal
620 slip and texture development in calcite: new results from torsion experiments,
621 *Phys. Chem. Miner.*, *34*, 73-84.
622 Barber, D. J., H. R. Wenk, and H. C. Heard (1994), The plastic deformation of
623 polycrystalline dolomite: comparison of experimental results of theoretical
624 predictions, *Mater. Sci. Eng. A, 175*, 83–104.
625 Bass, J. D. (1995), Elasticity of minerals, glasses and melts. In: Ahrens, T.J. (Ed.),
626 Mineral Physics and Crystallography, A Handbook of Physical Constants, AGU.,
627 Washington, D.C., pp. 45–63.
628 Bestmann, M., K. Kunze, and A. Matthews (2000), Evolution of a calcite marble shear
629 zone complex on Thassos Island, Greece: microstructural and textural fabrics and
630 theirkinematic significance, *J. Struct. Geol.*, *22*, 1789–1807.
631 Davis, N. E., A. K. Kronenberg, and J. Newman (2008), Plasticity and diffusion creep
632 of dolomite, *Tectonophysics, 456*, 127–146.
633 Davis, R. G., and N. S. Stoloff (1965), On the yield stress of aged Ni-Al alloys, *Trans.*
634 *Metall. Soc. AIME.*, *233*, 714-719.
635 de Bresser, J. H. P. (2002), On the mechanism of dislocation creep of calcite at high
636 temperature: Inferences from experimentally measured pressure sensitivity and
637 strain rate sensitivity of flow stress, *J. Geophys. Res. 107*, 1–16.
638 de Bresser, J. H. P., and C. J. Spiers (1997), Strength characteristics of the r, f, and c
639 slip systems in calcite, *Tectonophysics, 272*, 1-23.
640 de Bresser, J. H. P., J. L. Urai, and D. L. Olgaard (2005), Effect of water on the strength
641 and microstructure of Carrara marble axially compressed at high temperature, *J.*
642 *Struct. Geol.*, *27*(2), 265-281.
643 Delle Piane, C., L. Burlini, K. Kunze, P. Brack, and J. P. Burg (2008), Rheology of
644 dolomite: large strain torsion experiments and natural examples, *J. Struct. Geol.*,
645 *30*, 767–776.
646 Freund, D., Z. C. Wang, E. Rybacki, and D. Georg (2004), High-temperature creep of
647 synthetic calcite aggregates: influence of Mn-content, *Earth Planet. Sci. Lett.*,
648 *226*(3-4), 433-448.

649 Goldsmith, J. R. (1959), Some aspects of the geochemistry of carbonates, In: Abelson,
650 P.H. (Ed.), *Researches in Geochemistry, vol. 1*, pp. 336–358.
651 Goto, A., K. Kunugiza, and S. Omori (2007), Evolving fluid composition during
652 prograde metamorphism in subduction zones: A new approach using carbonate-
653 bearing assemblages in the pelitic system, *Gondwana Res., 11*(1-2), 166-179.
654 Gratier, J. P., J. Richard, F. Renard, et al., (2011), A seismic sliding of active faults by
655 pressure solution creep: evidence from the San Andreas Fault Observatory at
656 Depth, *Geology, 39*(12), 1131-1134.
657 Griggs, D., and W. B. Miller (1951), Deformation of Yule marble, part I. Compression
658 and extension on dry Yule marble at 10000 atmospheres confining pressure, room
659 temperature, *GSA Bulletin, 62*, 853–862.
660 Griggs, D. T., F. J. Turner, I. Borg, and J. Sosoka (1953), Deformation of Yule marble,
661 part V., effects at 300 °C, *GSA Bulletin, 64*, 1327-1342.
662 Handin, J., and H. W. Fairbairn (1955), Experimental deformation of Hasmark dolomite,
663 *GSA Bulletin, 66*, 1257-1274.
664 Handin, J., and D. Griggs (1951), Deformation of Yule marble, Part II., Predicted fabric
665 changes, *GSA Bulletin, 62*, 863-886.
666 Heard, H. C. (1976), Comparison of the flow properties of rocks at crustal conditions,
667 *Philosophical Transactions of the Royal Society of London, 283*, 173-186.
668 Heard, H. C., and C. B. Raleigh (1972), Steady-state flow in marble at 500 ° to 800 °C,
669 *GSA Bulletin, 83*, 935–956.
670 Herwegh, M., X. Xiao, and B. Evans (2003), The effect of dissolved magnesium on
671 diffusion creep in calcite, *Earth Planet. Sci. Lett., 212*(3), 457-470.
672 Herwegh, M., J. H. P. de Bresser, and J. H. ter Heege (2005), Combining natural
673 microstructures with composite flow laws: an improved approach for the
674 extrapolation of lab data to nature, *J. Struct. Geol., 27*, 503-521.
675 Higgs, D. V., and J. Handin (1959), Experimental deformation of dolomite single
676 crystals, *GSA Bulletin, 70*, 245–278.
677 Holyoke, C. W., A. K. Kronenberg, and J. Newman (2013), Dislocation creep of
678 polycrystalline dolomite, *Tectonophysics, 590*, 72-82.

679 Holyoke, C. W., A. K. Kronenberg, J. Newman, and C. Ulrich (2014), Rheology of
680 magnesite, *J. Geophys. Res., 119*, 6534-6557.
681 Karato, S. (2008), Deformation of Earth Materials: An Introduction to the Rheology of
682 Solid Earth, *Cambridge University Press*, 463.
683 Lawley, A., E. A. Vidoz, and R. W. Cahn (1961), The dependence of the flow stress of
684 Fe_3Al on crystallographic order, *Acta Metall., 9*, 287-296.
685 Li, J. F., M. S. Song, T. B. Shao, Y. Xia, Q. Wang, and W. Zhou (2013), Correction for
686 the axial deformation data recorded by Paterson-type gas medium high-pressure
687 high temperature machine, *Geotectonica et Metallogenia, 37*(1), 127-137 (in
688 Chinese with English abstract).
689 Neumann, E.-R. (1969), Experimental recrystallization of dolomite and comparison of
690 preferred orientations of calcite and dolomite in deformed rocks, *J. Geol., 77*, 426-
691 438.
692 Paterson, M. S. (1970), A high-pressure, high-temperature apparatus for rock
693 deformation, *International Journal of Rock Mechanics & Mining Science &*
694 *Geomechanics Abstracts, 7*(5), 517-526.
695 Poirier, J. P. (1985), Creep of Crystals: High-Temperature Deformation Processes in
696 Metals, Ceramics, and Minerals. *Cambridge University Press*, Cambridge, 260pp.
697 Renner, J., B. Evans, and G. Siddiqi (2002), Dislocation creep of calcite, *J. Geophys.*
698 *Res., 107*, 1-16.
699 Rutter, E. H. (1972), Influence of interstitial water on rheological behavior of calcite
700 rocks, *Tectonophysics, 14*, 13–33.
701 Rutter, E. H. (1974), Influence of temperature, strain rate and interstitial water in
702 experimental deformation of calcite rocks, *Tectonophysics, 22*, 311–334.
703 Rybacki, E., C. Janssen, R. Wirth, K. Chen, H.-R. Wenk, D. Stromeyer, and G. Dresen
704 (2011), Low-temperature deformation in calcite veins of SAFOD core samples
705 (San Andreas Fault)-Microstructural analysis and implications for fault rheology,
706 *Tectonophysics, 509*(1-2), 107-119.
707 Rybacki, E., B. Evan, C. Janssen, R. Wirth, and G. Dresen (2013), Influence of stress,
708 temperature, and strain on calcite twins constrained by deformation experiments,

709 *Tectonophysics, 601*, 20-36.
710 Schmid, S., J. N. Boland, and M. S. Paterson (1977), Super-plastic flow in fine-grained
711 limestone, *Tectonophysics*, *43*, 257–292.
712 Schmid, S., M. S. Paterson, and J. N. Boland (1980), High temperature flow and
713 dynamic recrystallization in Carrara marble, *Tectonophysics*, *65*, 245–280.
714 Shao, T.B, S. C. Ji, J. F. Li, Q. Wang, and M. S. Song (2011), Paterson gas-medium
715 high-pressure high-temperature testing system and its applications in rheology of
716 rocks, *Geotectonica et Metallogenia, 35*(3), 457-476 (in Chinese with English
717 abstract).
718 Song, M. S., T. B. Shao, J. F. Li, S. C. Ji, and Q. Wang (2014), Experimental study of
719 deformation of Carrara marble at high pressure and high temperature, *Acta*
720 *Petrologica Sinica*, *30*(2), 589-596 (in Chinese with English abstract).
721 Stoloff, N. S., and R. G. Davies (1964), The effect of ordering on the plastic
722 deformation of Mg_3Cd, *Trans. Am. Soc. Met.*, *57*, 247-260.
723 Turner, F. J., D. T. Griggs, R. H. Clark, and R. H. Dixon (1956), Deformation of Yule
724 marble, part VII: development of oriented fabrics at 300 °C-500 °C, *GSA Bulletin*,
725 *67*, 1259–1294.
726 Turner, F. J., D. T. Griggs, H. Heard, and L. W. Weiss (1954), Plastic deformation of
727 dolomite rock at 380 °C, *Am. J. Sci., 252*, 477–488.
728 Ulrich, S., K. Schumann, and M. Casey (2002), Microstructural evolution and
729 rheological behavior of marbles deformed at different crustal levels, *J. Struct.*
730 *Geol., 24*, 979-995.
731 Walker, A. N., E. H. Rutter, and K. H. Brodie (1990), Experimental study of grain-size
732 sensitive flow of synthetic, hot-pressed calcite rocks, In: Knipe, R.J., Rutter, E.H.
733 (Eds.), Deformation Mechanisms, Rheology and Tectonics, *Spec. Publ. Geol. Soc.*,
734 *54*, 259–284.
735 Wright, R. N. (2016), Chapter 11 – Mechanical Properties of Wire and Related Testing,
736 in Wire Technology (Second Edition), *Process Engineering and Metallurgy*, 129-
737 157.
738 Wyllie, P. J. and W. L. Huang (1976), Carbonation and melting reactions in the system

739 CaO-MgO-SiO_2-CO_2 at mantle pressures with geophysical and petrological
740 applications, *Contrib. Miner. Petrol., 54*, 79-107.
741 Xu, L. L., and B. Evans (2010), Strain heterogeneity in deformed Carrara marble using
742 a microscale strain mapping technique, *J. Geophys. Res., 115*(B4), B04202.
743 Xu, L. L., J. Renner, M. Herwegh, and B. Evans (2009), The effect of dissolved
744 magnesium on creep of calcite II: transition from diffusion creep to dislocation
745 creep, *Contrib. Miner. Petrol., 157*(3), 339-358.
746 Zhang, L., D. J. Ellis, R. J. Arculus, W. Jiang, and C. Wei (2003), 'Forbidden zone'
747 subduction of sediments to 150 km depth – The reaction of dolomite to magnesite
748 plus aragonite in the UHPM metapelites from western Tianshan, China, *J.*
749 *Metamorph. Geol., 21*, 523-529.
750 Zhang, Y. H., Y. S. Zhou, W. M. Yao, C. R. He, and J. X. Dang (2017), Experimental
751 study on the effect of water on the strength and deformation mechanism of Carrara
752 marble at high temperature, *Seismology and Geology, 39*(1), doi:10.3969/
753 j.issn.0253-4967.2017.01 (in Chinese with English abstract).
754 Zhang, Y. Y., and Y. S. Zhou (2012), The strength and deformation mechanisms of
755 brittle-plastic transition zone, and the effects of strain rate and fluids, *Seismology*
756 *and Geology, 34*(1), 172-194 (in Chinese with English abstract).

Figure captions

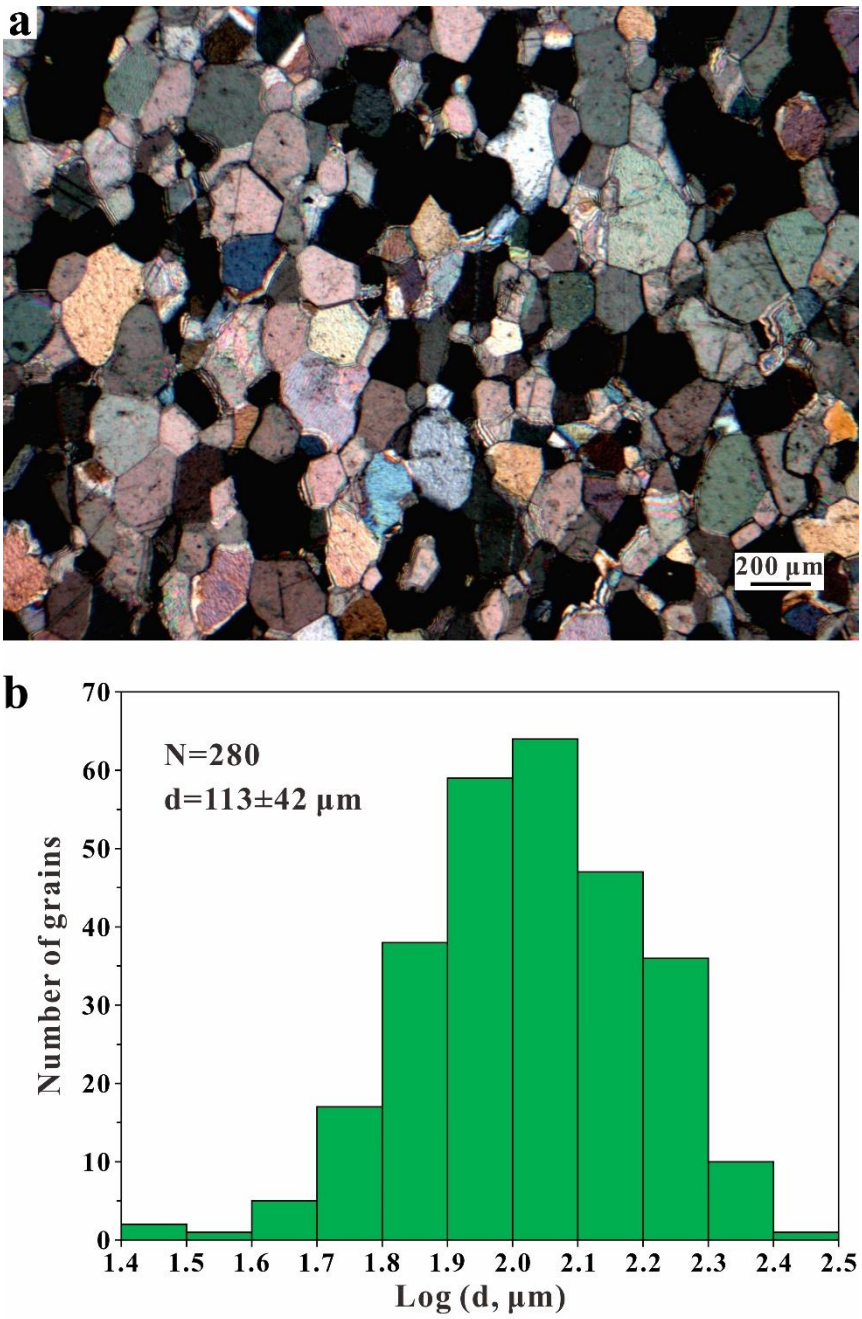

Figure 1. Orthogonal optical micrograph (a) and frequency diagram of grain diameter (b) show that the starting materials (Fangshan dolomites) have approximately equant grains with diameter ~113 µm and are characterized by sharp grain boundaries, uniform extinction, and some twin.

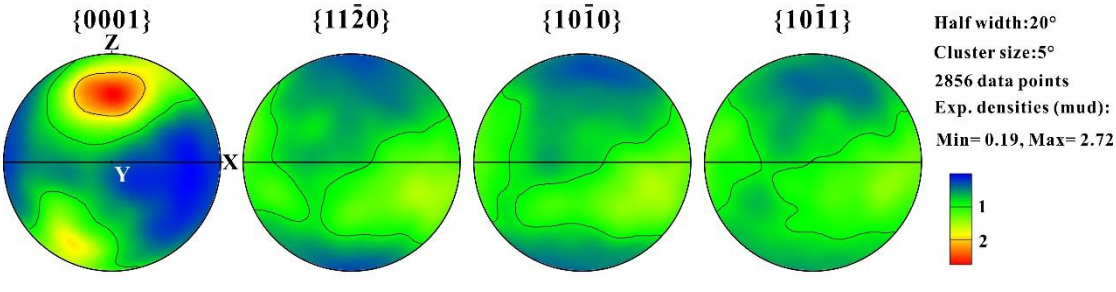

764

765 **Figure 2.** Pole figures of starting materials indicative of a weak fabric of c-axis

766

767

768

769

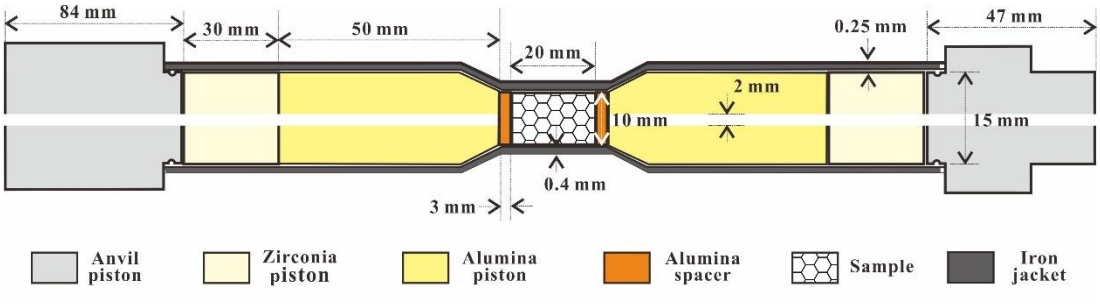

770

771 **Figure 3.** Schematic illustration of specimen assembly for triaxial compression

772 experiments in a Paterson-type deformation apparatus

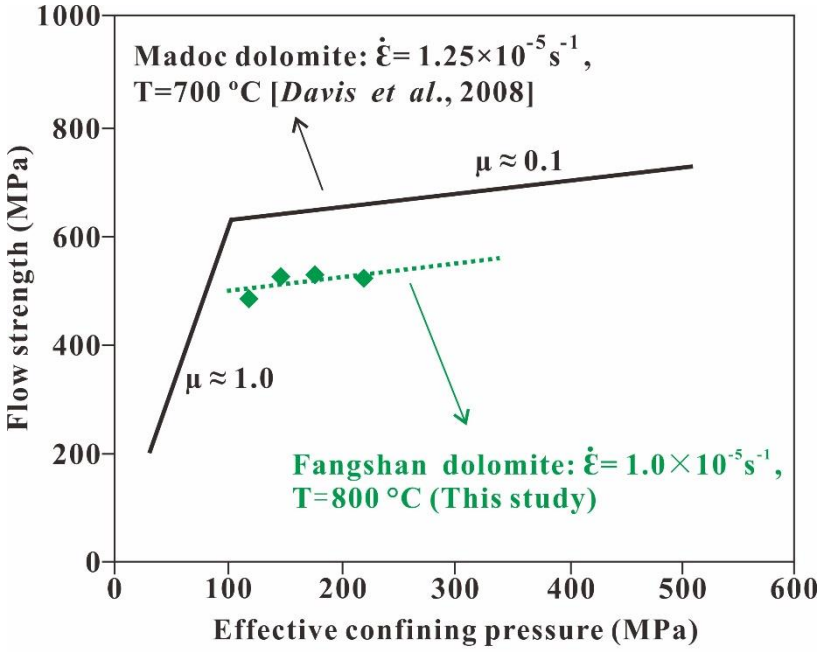

Figure 4. Effective pressure (P_e) dependence of flow strength of polycrystalline dolomite. Black lines are obtained by fitting flow strength to effective pressure of data on coarse-grained Madoc dolomite deformed at 700 ℃ and 1.25×10^{-5} s^{-1} from *Davis et al*. [2008]. Specifically, the flow strength of Madoc dolomite is linearly dependent on effective pressure with a tiny apparent coefficient of inner friction about 0.1 ($\mu \cong 0.1$) if deformed at $P_e > 100$ MPa, 700 ℃ and strain rate of 1.25×10^{-5} s^{-1}, while if $P_e <$ 100 MPa the dependence of flow strength on effective pressure meets the Mohr – Coulumb Criterion with an apparent coefficient of inner friction about 1.0 ($\mu \cong 1.0$). Green diamonds represent the data of medium-grained Fangshan dolomite compressed at 800 ℃ and 1.0×10^{-5} s^{-1}, to which a green line is fitted showing a weak dependence of flow strength on effective pressure with an apparent inner friction coefficient equal to 0.1.

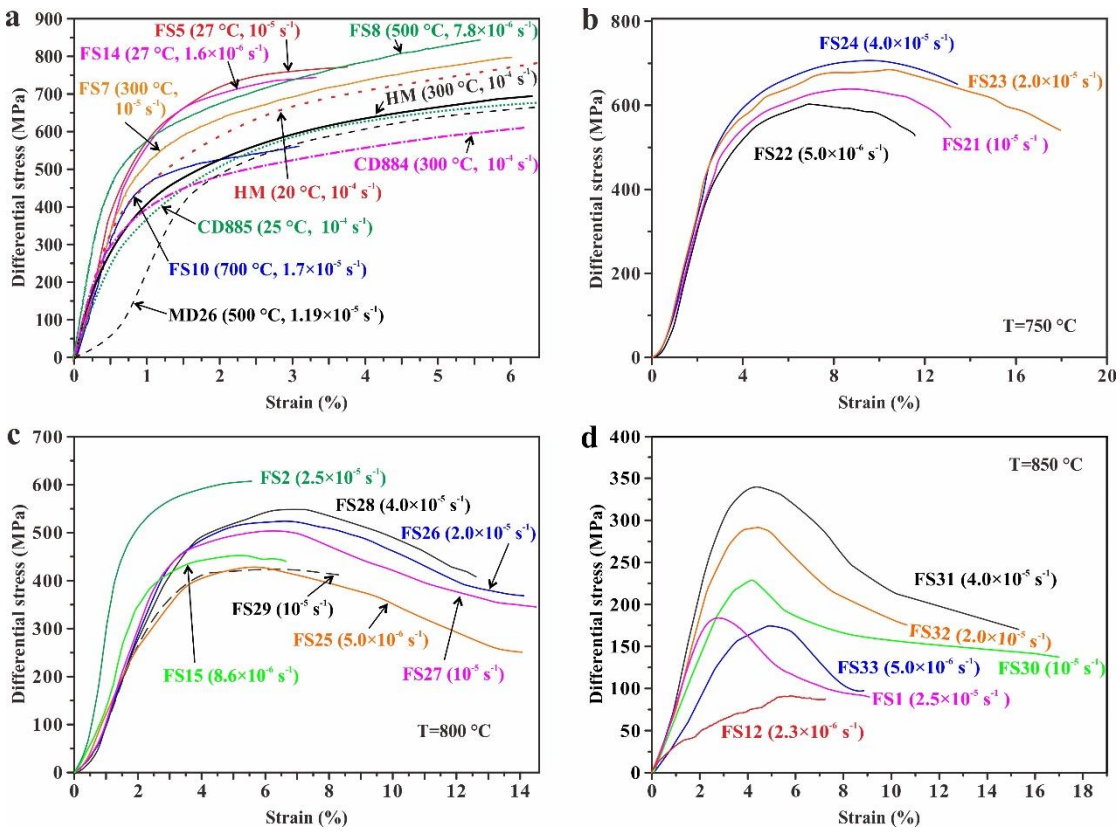

Figure 5. Differential stress versus strain curves of dolomite compressed at individual constant strain rates. HM, CD, and MD26 in Figure 5a are compilation of previous results for Hasmark dolomite [T-cylinders, *Handin and Fairbairn*, 1955], Crevola dolomite [*Barber et al.*, 1994], and Madoc dolomite [*Davis et al.*, 2008], respectively, obtained at a strain rate of 10^{-4} s^{-1}. The effective confining pressures for our all tests are 50-300 MPa. Respective strain rate and temperature or alone strain rate at a constant temperature are marked after each sample name.

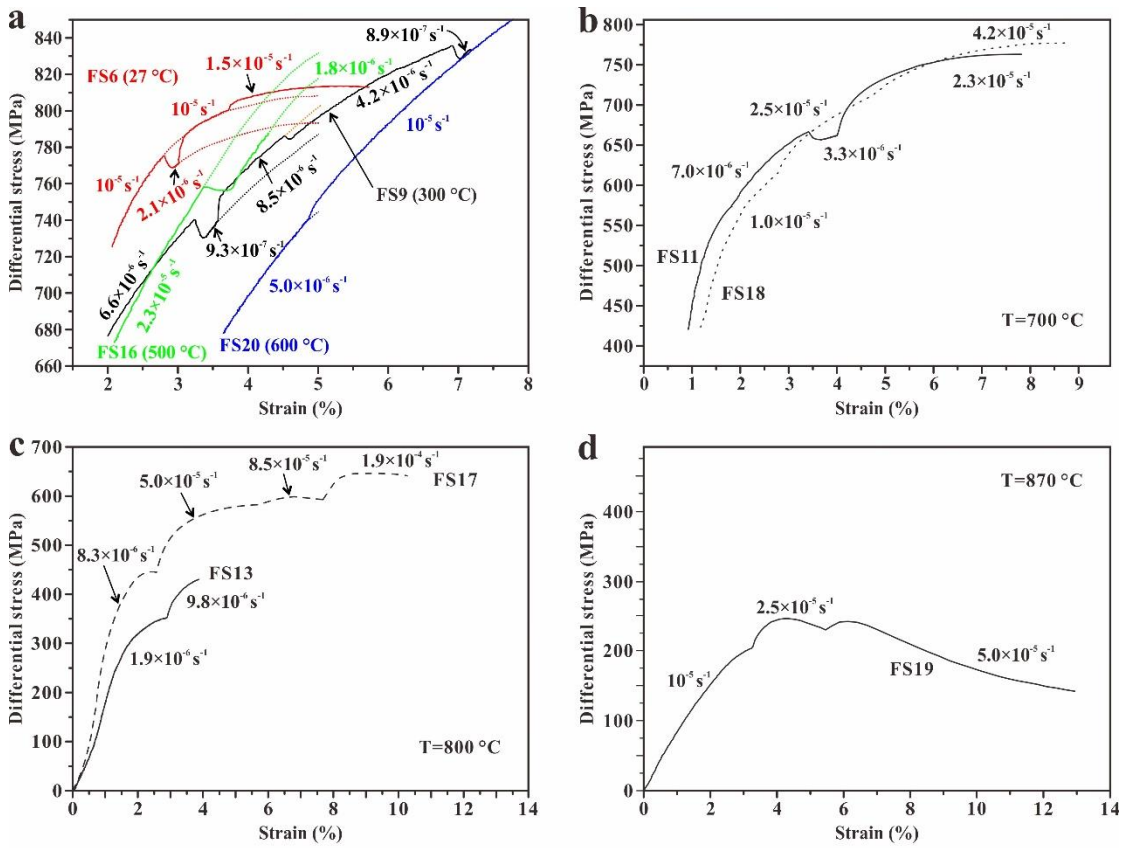

Figure 6. Differential stress versus strain curves of Fangshan dolomite compressed in strain-rate-stepping experiments. The effective confining pressures for all tests are 50-300 MPa. Strain rates are marked along or with arrows pointing to each stage of curve. In Figure a, curves of different samples (temperatures) are marked in different color, dotted line represents the extension of curve under a strain rate.

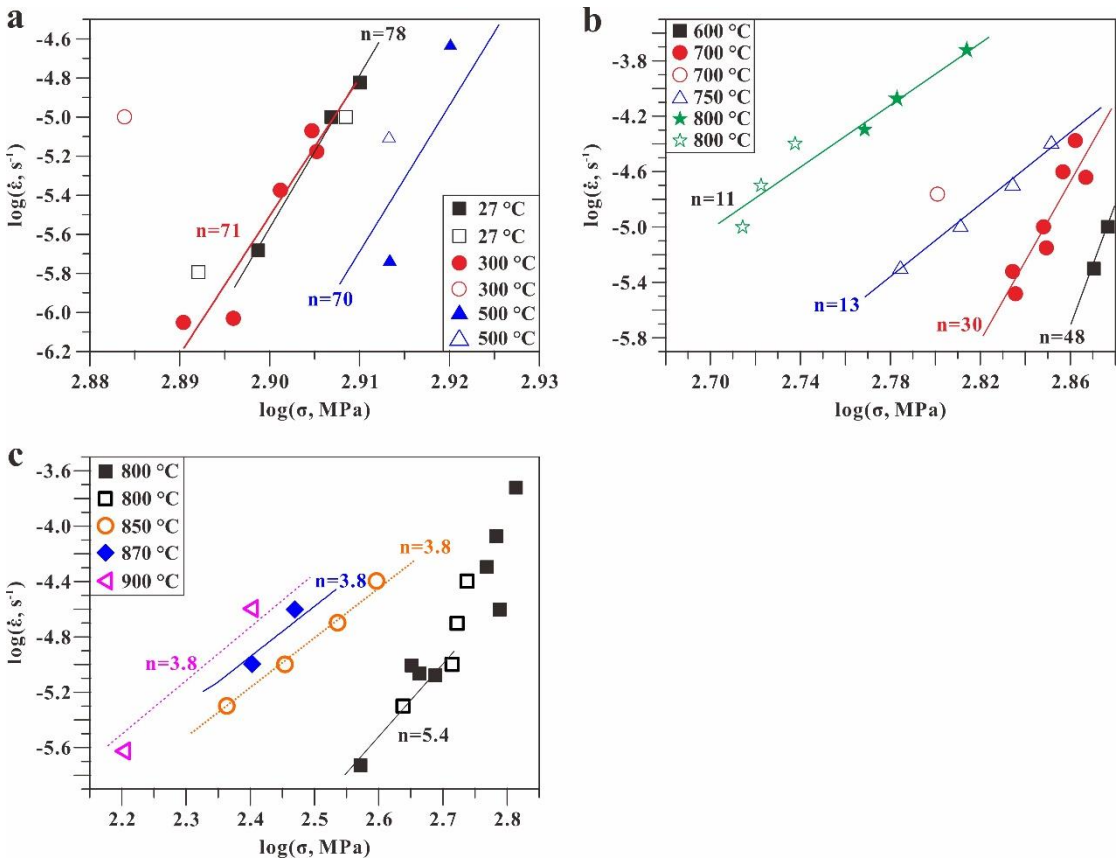

Figure 7. $\log\dot{\varepsilon}$ versus $\log\sigma$ plots for Fangshan dolomites deformed in three regimes. Note: The confining pressures of all tests are 300 MPa. a – Regime 1 at temperature ≤500℃ with extremely high stress exponents (n=~70), indicating obviously weak dependence of flow strength on strain rate; b - Regime 3 at temperature from 600 ℃ to 750 ℃ with moderate and gradually decreasing stress exponents (n value of 48 to 13); c – Regime 2 at temperatures higher than 800℃ and/or equal to 800 ºC but with flow strength lower than 520 MPa is characterized by significantly low stress exponents, whose values are basically consistent with those expected for dislocation creep. Solid symbols represent data collected from strain-rate-stepping experiments, while hollow symbols represent data collect from individual constant strain rate tests.

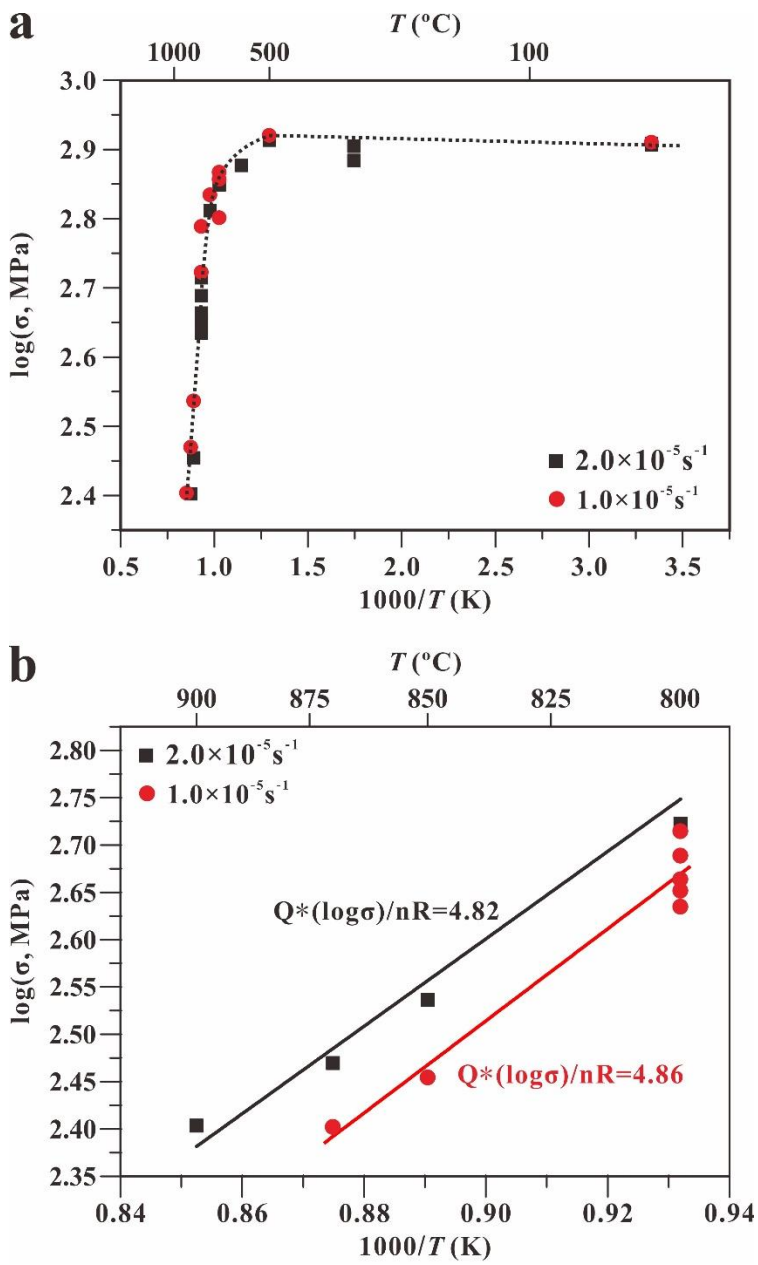

Figure 8. logσ versus 1000/T plots of experimental results displaying strength of medium-grained Fangshan dolomite as a function of temperature. (a) At low temperatures (≤500 ºC), strengths of medium-grained Fangshan dolomite are insensitive to temperature and increase very slightly with increasing temperature. At moderate temperatures (500 ºC<T<~750 ºC), strengths are much more insensitive to temperature and decrease significantly with increasing temperature. At high temperatures (≥~750 ºC), strengths decrease sharply with increasing temperature. (b) At higher temperatures (800 ºC≤T≤900 ºC), fittings of logσ versus 1000/T at two different strain rates result in a similar slope given by Q*(logσ)/nR=4.8.

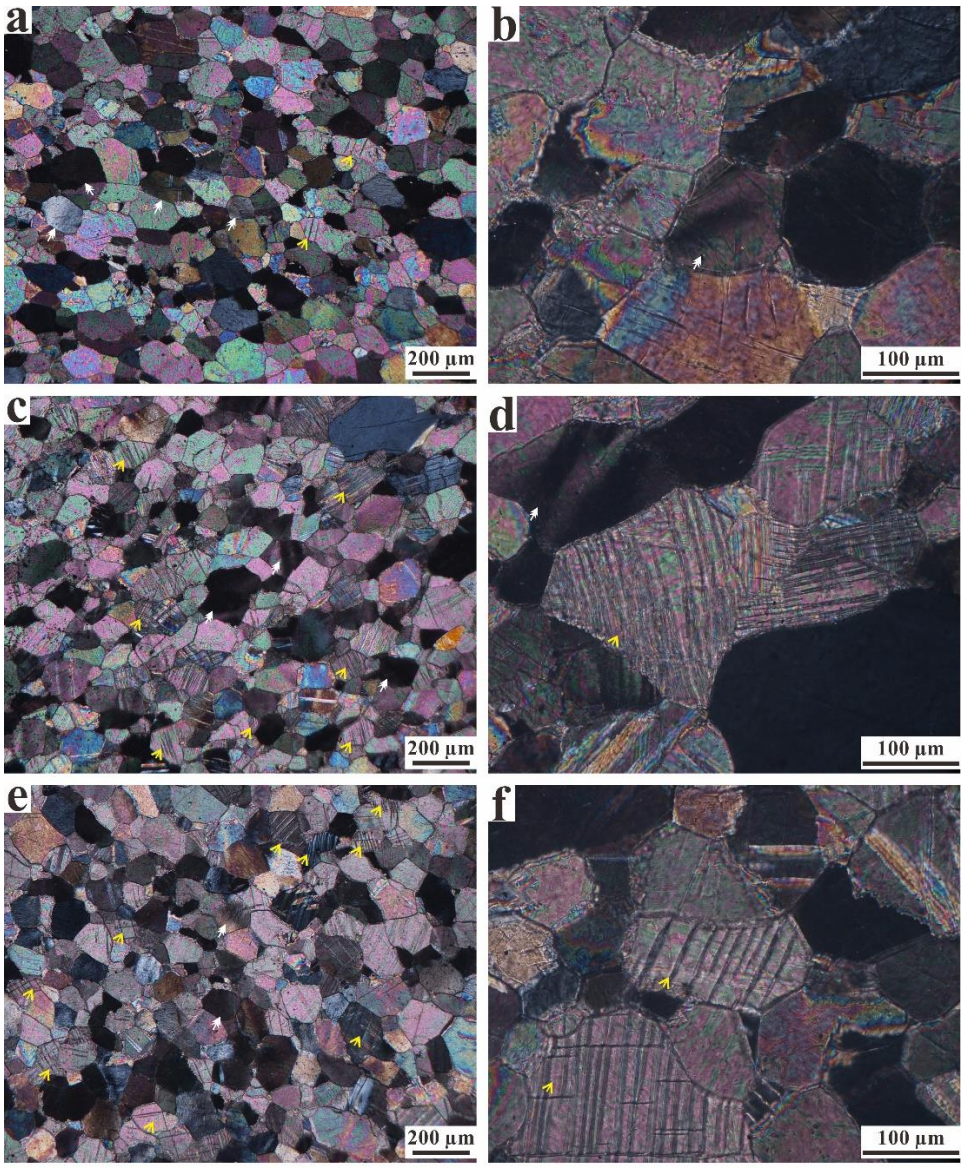

Figure 9. Optical microstructures of medium-grained Fangshan dolomite, deformed at temperatures ≤ 500 ℃, in cross-polarized light. (a and b) Undulatory extinction and extinction bands developed in the Fangshan dolomite deformed at room temperature; (a) sample FS14 deformed at room temperature and a constant strain rate of 1.6×10^{-6} s^{-1} to a total strain of 3.65; (b) sample FS6 deformed at room temperature and stepping strain rates to a total strain of 6.29%. (c and d) Both undulatory extinction and f – twins were pervasive in the Fangshan dolomites (sample FS9) deformed at 300 ℃ and stepping strain rates to a total strain of 7.18% (e and f) f twinning became dominant in the Fangshan dolomites (sample FS8) at 500 ℃ and 7.8×10^{-6} s^{-1} to a total strain of 7%. The undulatory extinctions were represented by white arrows, while mechanical twins were marked by yellow arrows.

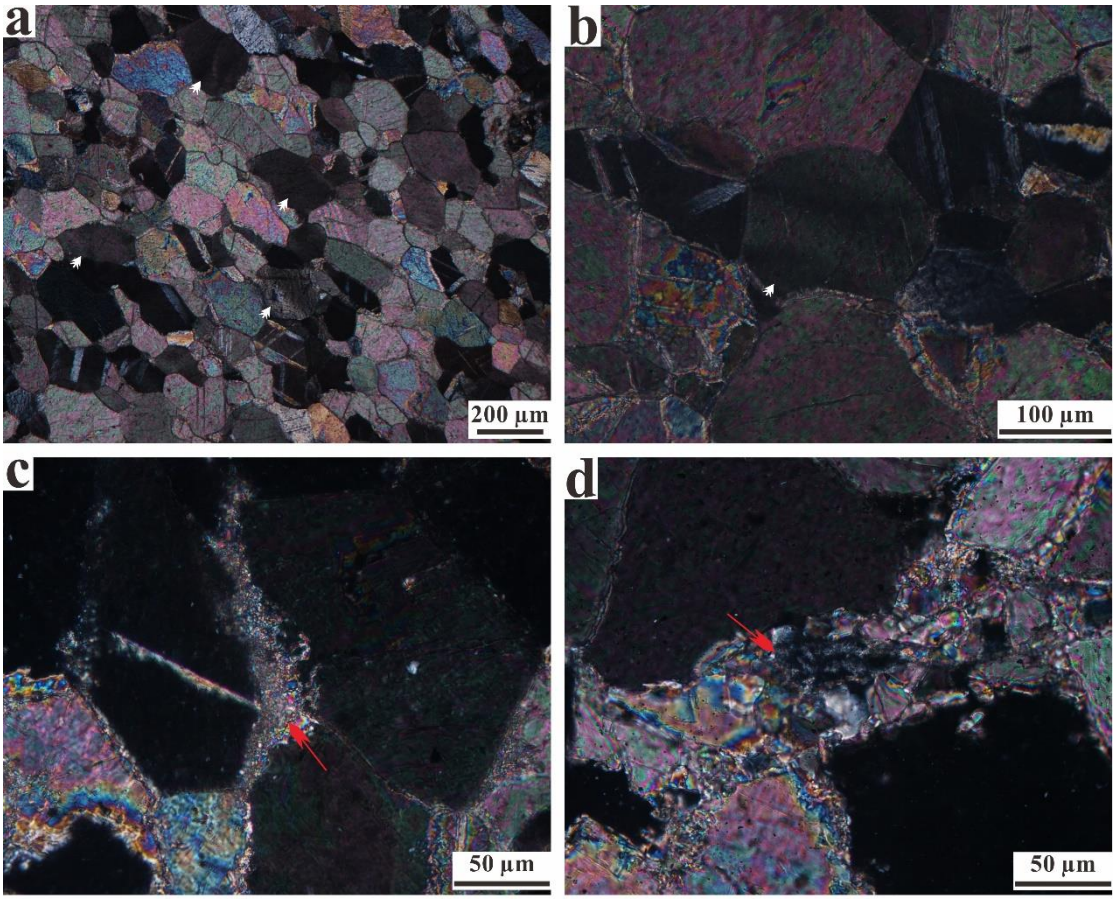

Figure 10. Optical microstructures of medium-grained Fangshan dolomite, deformed at temperatures ≥ 700 ℃, in cross-polarized light. (a and b) Smooth undulating extinctions developed in the Fangshan dolomites (sample FS15) deformed at temperature ≥800 ℃ and stepping strain rates to a total strain of 11.1%. (c and d) Some new fine grains were discovered at the triple junction of dolomite grains or surrounding the accessory minerals such as mica and apatite in samples FS15 (c) and FS12 (d), the latter of which were deformed at 900 ºC and 2.3×10^{-6} s^{-1} to a total strain of 7.27%. The undulatory extinctions were represented by white arrows, while the new fine grains formed by decomposition of dolomite were marked by red arrows.

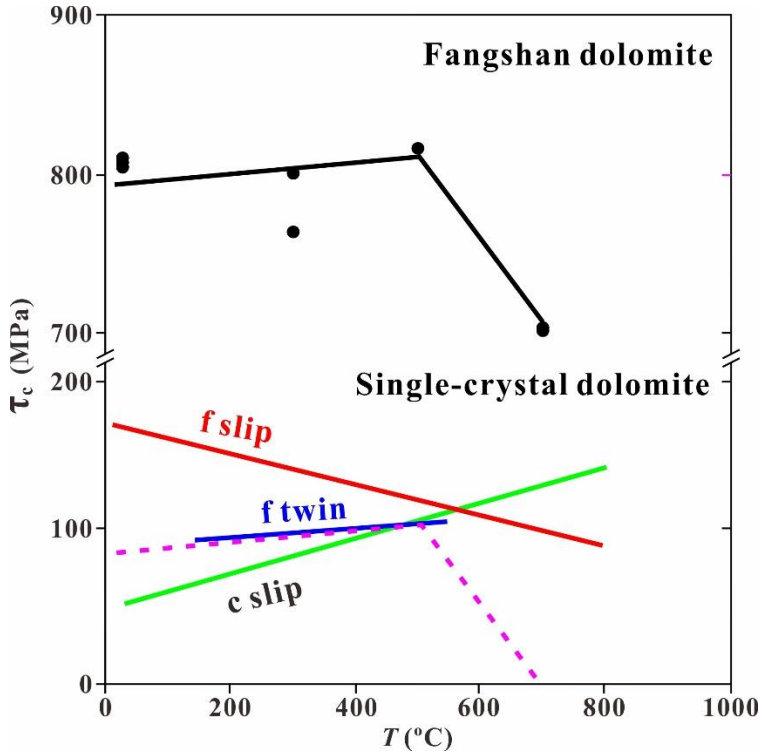

Figure 11. Critical resolved shear stress (CRSS) for dominant slip and twin systems in single-crystal dolomite [*Barber et al.*, 1981] and polycrystalline Fangshan dolomites. The temperature dependence trends of flow strength of the Fangshan dolomite were consistent with a transition for single-crystal dolomite from c slip dominant at room temperature to f twinning dominant at 500 ℃, and then to dislocation creep dominant deformation mechanism at temperature higher than 700 ℃. Pink dotted line is formed by the translation of the black solid line.

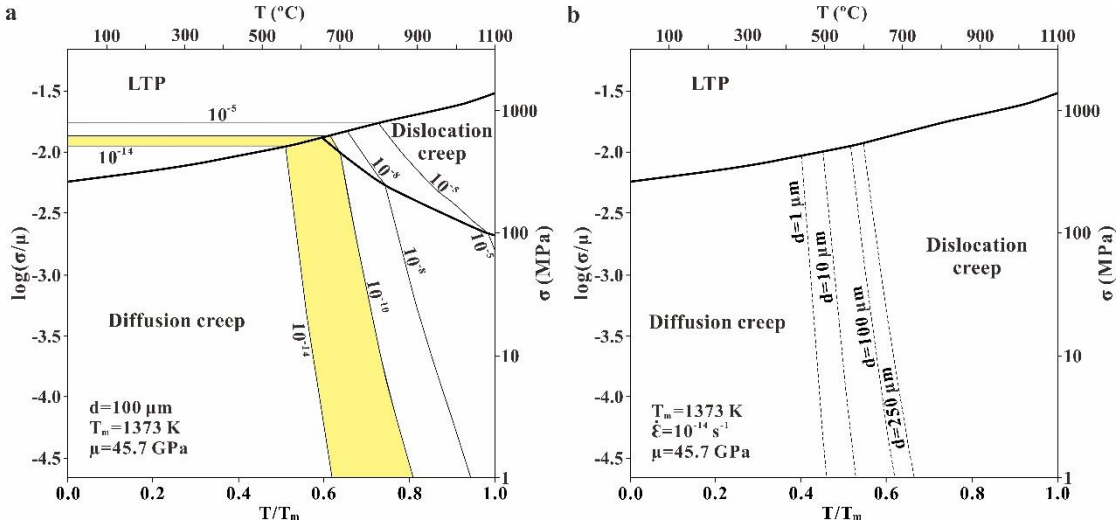

Figure 12. (a) A deformation mechanism map constructed using the low temperature plasticity (LTP) and dislocation creep flow laws of this study and the diffusion creep flow law of *Davis et al*. [2008] suggests that naturally-deformed, medium-grained (100 μm) dolomite aggregates deformed over most geological strain rates (10^{-10}-10^{-14} s^{-1}), LTP dominates at temperatures not higher than ~560 ºC. At temperatures between 560 ºC and 650 ºC, the deformation of dolomites is dominated by LTP at relatively high differential stresses and by diffusion creep at low stresses. When T>650 ºC, however, diffusion creep is the dominant deformation mechanism, likely accompanied by LTP and dislocation creep accommodating very small amount strain. (b) Changing grain size of dolomite shifts the dislocation creep-diffusion creep boundary to lower temperatures when refining or to higher temperatures when coarsening. Temperature is normalized by a melting temperature [T_m=1373 K, metastable extension from high pressure measurements, *Wyllie and Huang*, 1976], and flow strength is normalized by a shear modulus [μ=45.7 GPa, *Bass*, 1995].

Table 1. Chemical composition (wt.%) of Fangshan dolomite

Point#	MgO	CaO	FeO	Al_2O_3	Na_2O	MnO	P_2O_5	TiO_2	Total	Mg/Ca
1	20.61	29.88	0.12	0.00	0.02	0.00	0.01	0.00	50.65	0.97
2	21.18	30.25	0.11	0.02	0.04	0.00	0.01	0.03	51.64	0.98
3	21.41	29.38	0.11	0.02	0.07	0.03	0.00	0.00	51.02	1.02

Table 2. Experimental conditions and mechanical results of constant strain rate tests on Fangshan dolomite

Run#	Confining pressure	Effective pressure	Temperature	Strain rate	Strain corresponding to peak strength	Peak strength	Flow strength	Correctived by P_e	Total strian
	P_c	P_e	T			σ_P	$\sigma_{5\%}$		ε_T
	MPa	MPa	ºC	sec^{-1}	%	MPa	MPa		%
FS5	300	300	27	1.0×10^{-5}	3.0	783.82	810.00		3.1
FS14	300	300	27	1.6×10^{-6}		NA	780.00		3.7
FS7	300	300	300	1.0×10^{-5}		NA	765.35		6.4
FS8	300	300	500	7.8×10^{-6}		NA	819.01		7.0
FS10	300	270	700	1.7×10^{-5}		NA	629.48	632.48	3.5
FS21	300	250	750	1.0×10^{-5}	8.1	642.45		647.45	13.2
FS22	300	250	750	5.0×10^{-6}	7.1	603.74		608.74	11.6
FS23	300	250	750	2.0×10^{-5}	8.1	677.89		682.89	18.0
FS24	300	250	750	4.0×10^{-5}	9.6	705.53		710.53	13.5
FS2	300	220	800	2.5×10^{-5}	5.6	609.10	606.70	614.70	7.6
FS25	300	220	800	5.0×10^{-6}	5.9	426.48		434.48	14.1
FS26	300	220	800	2.0×10^{-5}	5.9	519.87		527.87	13.8
FS27	300	220	800	1.0×10^{-5}	5.4	509.98		517.98	14.5
FS28	300	220	800	4.0×10^{-5}	6.8	538.59		546.59	12.7
FS29	300	220	800	1.0×10^{-5}	6.0	423.18		431.18	9.8
FS30	260	60	850	1.0×10^{-5}	4.2	228.54		284.54	17.1
FS31	260	60	850	4.0×10^{-5}	4.4	339.28		395.28	15.1
FS32	260	60	850	2.0×10^{-5}	4.8	287.81		343.81	10.5
FS33	260	60	850	5.0×10^{-6}	5.0	175.12		231.12	9.5
FS1	300	50	900	2.5×10^{-5}	2.8	183.15	NA*	253.15	9.0
FS12	300	50	900	2.3×10^{-6}	5.8	90.05	83.63	160.05	7.3

*NA=Not achieved

Table 3. Experimental conditions and mechanical results of strain-rate-stepping tests on Fangshan dolomite

Run#	Confining pressure P_c MPa	Effctive pressure P_e MPa	Temperature T ºC	Strain rate sec^{-1}	Flow strength $\sigma_{5\%}$ MPa	Correctived by P_e MPa	Total strian ε_T %
FS6	300	300	27	1.0×10^{-5}	807.00		
				2.1×10^{-6}	792.00		
				1.0×10^{-5}	807.00		
				1.5×10^{-5}	812.96		6.3
FS9	300	300	300	6.6×10^{-6}	804.00		
				9.3×10^{-7}	787.00		
				8.5×10^{-6}	803.00		
				4.2×10^{-6}	796.54		
				8.9×10^{-7}	777.00		7.2
FS16	300	300	500	1.8×10^{-6}	819.14		
				2.3×10^{-5}	832.00		
FS20	300		600	5.0×10^{-6}	742.17		
				1.0×10^{-5}	752.80		9.1
FS11	300	270	700	7.0×10^{-6}	704.00	707.00	
				3.3×10^{-6}	682.00	685.00	
				2.3×10^{-5}	733.12	736.12	9.4
FS18	300	270	700	4.8×10^{-6}	680.00	683.00	
				1.0×10^{-5}	702.00	705.00	
				2.5×10^{-5}	716.00	719.00	
				4.2×10^{-5}	725.25	728.25	
FS13	300	220	800	1.9×10^{-6}	365.00	373.00	
				9.8×10^{-6}	440.32	448.32	7.8
FS15	300	220	800	8.6×10^{-6}	452.66	460.66	
				3.1×10^{-6}	NA*		11.1
FS17	300	220	800	8.3×10^{-6}	480.00	488.00	
				5.1×10^{-5}	578.95	586.95	
				8.5×10^{-5}	598.72	606.72	6.8
				1.9×10^{-4}	643.56	651.56	8.8
FS19	300	70	870	1.0×10^{-5}	202.38	252.38	3.2
				2.5×10^{-5}	244.77	294.77	4.1
				5.0×10^{-5}	NA*		12.9
FS34	257	177	800	1.0×10^{-5}	515.70	523.7	
	227	147	800	1.0×10^{-5}	512.26	520.26	
	199	119	800	1.0×10^{-5}	472.44	480.44	

*NA=Not achieved